

# A Robust Automatic Nuclei Segmentation Technique for Quantitative Histopathological Image Analysis

**Cheng Lu, M.Sc., Muhammad Mahmood, M.D., Naresh Jha, M.D., and Mrinal Mandal, Ph.D.**

**OBJECTIVE:** To develop a computer-aided robust nuclei segmentation technique for quantitative histopathological image analysis.

**STUDY DESIGN:** A robust nuclei segmentation technique for histopathological image analysis is proposed. The proposed technique uses a hybrid morphological reconstruction module to reduce the intensity variation within the nuclei regions and suppress the noise in the image. A local region adaptive threshold selection module, based on local optimal threshold is used to segment the nuclei. The technique incorporates domain-specific knowledge of skin histopathological images for a more accurate segmentation results.

**RESULTS:** The technique is compared to the manually labeled nuclei locations and nuclei boundaries for the performance evaluations. On different histopathological images of skin epidermis with complex background, containing more than 3000 nuclei, the technique provides a good nuclei detection performance: 88.11% sensitivity rate, 80.02% positive prediction rate and only 5.34% under-segmentation rate compared to the manually labeled nuclei locations. Compared to the 110 manually segmented nuclei regions, the proposed technique provides a good segmentation performance (in terms of the nucleus area, perimeter, and form factor).

**CONCLUSION:** The proposed technique is able to provide more accurate segmentation performance compared to the existing techniques and can be employed for quantitative analysis of the histopathological images. (Anal Quant Cytopathol Histopathol 2012;34:000–000)

**Keywords:** adaptive thresholding, computer-assisted image analysis, histopathological image analysis, nuclei segmentation, skin histopathological image.

Microscopic analysis of hematoxylin and eosin (H&E)-stained sections forms the backbone of most diagnoses rendered by anatomical pathologists. Among other parameters, evaluation of cell nuclei plays an important role in the histopathological examination and analysis. Anatomical pathologists, especially cytopathologists, give special attention to parameters like size, shape, contours and presence or absence of nucleoli and mitotic figures in nuclei. The morphological features and the distribution of the cell nuclei have great diagnostic value and play a very important role in determining the malignant nature of a lesion. Recently, in the environment of very efficient image based computer models, many

---

From the Department of Electrical and Computer Engineering, University of Alberta, Edmonton; the Division of Anatomical Pathology, Walter Mackenzie Health Sciences Center, Edmonton; and the Department of Oncology, University of Alberta, Cross Cancer Institute, Edmonton, Alberta, Canada.

Mr. Lu is Ph.D. Candidate, Department of Electrical and Computer Engineering, University of Alberta.

Dr. Mahmood is Assistant Professor, Division of Anatomical Pathology, Walter Mackenzie Health Sciences Center.

Dr. Jha is Professor, Department of Oncology, University of Alberta, Cross Cancer Institute.

Dr. Mandal is Professor, Department of Electrical and Computer Engineering, University of Alberta.

Address correspondence to Mrinal Mandal, Ph.D., Department of Electrical and Computer Engineering, University of Alberta, Edmonton, Alberta T6G 2V4, Canada (mmandal@ualberta.ca).

*Financial Disclosure:* The authors have no connection to any companies or products mentioned in this article.

computer-aided image analysis techniques have been proposed to evaluate and analyze cell nuclei (e.g., karyometric analysis<sup>1</sup>). In these computerized quantitative histopathological image analyses, the segmentation of cell nuclei is the first major step.<sup>2,3</sup> The accuracy of the automated segmentation technique employed is critical in obtaining good and efficient diagnostic performance.

Many different techniques have been tried for accurate segmentation of nuclei. Threshold-based techniques have been widely used for nuclei segmentation in histopathological images.<sup>1,4,5</sup> Gurcan et al<sup>4</sup> proposed a hysteresis threshold-based technique (HTWS) for nuclei segmentation in neuroblastoma images. Korde et al<sup>1</sup> proposed a global threshold-based technique (GT) to segment the nuclei in bladder and skin microscopic images. Petushi et al<sup>5</sup> proposed to use adaptive threshold (AT) for nuclei segmentation in the breast carcinoma histopathological images. Of note, the above-mentioned threshold-based techniques sometimes led to under-segmentation (the segmented object contains more than 1 desired object) or missed detection, especially if considerable intensity variations existed. Another method of nuclei segmentation utilized the probabilistic model to classify the pixels into 2 classes of foreground and background.<sup>6-8</sup> Geometric active contour (GAC) had also been applied in the nuclei segmentation problems. Fatakdawala et al<sup>9</sup> proposed to use GAC for the nuclei segmentation in breast carcinoma cases. However, the performance of this technique was sensitive to initialization and local intensity variations. In cases where the background and the foreground objects had similar intensity value, it was difficult to achieve good results. It was also computationally expensive.

In our study we propose an effective technique for segmentation of nuclei from histopathological images. Our technique overcomes many limitations of the aforementioned techniques and provides a superior performance by incorporating the domain knowledge.

## Materials and Methods

### Image Data

In this study we used a new technique on 30 different cutaneous histopathological images. The images are of the entire thickness of epidermis with the image having a size of 512×512 pixels. In these images the background and foreground are similar in terms of the color/intensity, however, some

staining variations can be observed. The histological sections used for image acquisition are prepared from formalin-fixed, paraffin-embedded tissue blocks of skin biopsies. The sections prepared are about 4 μm thick each and are stained with H&E using an automated stainer. The skin biopsies used contained normal skin, melanocytic nevi and melanomas. These digital images were captured under 30× magnification on a Carl Zeiss MIRAX MIDI Scanning system (Carl Zeiss Inc., Germany).

### Overall Schematic of the Proposed Technique

The schematic for the proposed technique is shown in Figure 1. There are 2 modules. The hybrid gray-scale morphological reconstructions (HGMR) module is used to reduce the undesired intensity variation in the image. Following that, the local region adaptive threshold selection (LRATS) module is next used to segment the nuclei.

### Hybrid Gray-scale Morphological Reconstructions

Due to the staining imperfection and variations, the appearance of the nuclei is generally not homogeneous. In order to reduce the influence from undesirable variations within the nuclei region, the HGMR is used to enhance the image. The steps of HGMR are described below.

- Complement of the Image.* Since the nuclei regions appear darker, we first calculate the complement of the image  $R$ , assuming an 8-bit image, as follows:

$$\bar{R}(x, y) = 255 - R(x, y) \quad (1)$$

where  $(x, y)$  is the coordinate.

- Opening-by-Reconstruction.* In order to enhance the nuclei regions, the opening-by-reconstruction operation<sup>10</sup> is performed on the image  $\bar{R}$  as follows:

$$\bar{R}_{obr} = \mathfrak{R}(\bar{R}_e, \bar{R}) \quad (2)$$

where  $\mathfrak{R}$  is the morphological reconstruction operator,<sup>10</sup>  $\bar{R}_e = \bar{R} \Theta S$  ( $\Theta$  is the erosion operator), and  $S$  is the structure element. We define the structure element as blob-like elements mainly because the

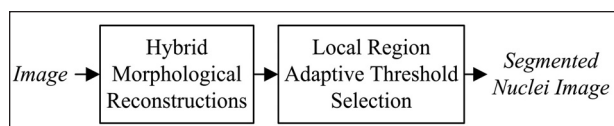


**Figure 1** The schematic for the proposed technique.

nuclei regions have a blob-like shape. The radius of the element is empirically set to 3 pixels for the  $30 \times$  magnification image. As a result, the structure element  $S$  is a  $7 \times 7$  rectangular function with tapered corners. This is expressed as follows:

$$S = \begin{bmatrix} 0 & 0 & 1 & 1 & 1 & 0 & 0 \\ 0 & 1 & 1 & 1 & 1 & 1 & 0 \\ 1 & 1 & 1 & 1 & 1 & 1 & 1 \\ 1 & 1 & 1 & 1 & 1 & 1 & 1 \\ 1 & 1 & 1 & 1 & 1 & 1 & 1 \\ 0 & 1 & 1 & 1 & 1 & 1 & 0 \\ 0 & 0 & 1 & 1 & 1 & 0 & 0 \end{bmatrix}. \quad (3)$$

*3. Closing-by-Reconstruction.* In order to reduce the noise further, the closing-by-reconstruction is performed on  $\bar{R}_{obr}$  as follows:

$$\bar{R}_{obrcbr} = 255 - \Re(R_{obr} \Theta S, R_{obr}) \quad (4)$$

where  $R_{obr} = 255 - \bar{R}_{obr}$ .

*4. Complement of the Image.* This step calculates the complement of  $\bar{R}_{obrcbr}$  in order to map the image into the original intensity space, i.e.,  $R'(x, y) = 255 - \bar{R}_{obrcbr}(x, y)$ .

#### Segmentation of the Nuclei Using LRATS

Following HGMR, segmentation of nuclei is performed using the LRATS module. The 2 steps involved are described as follows:

*1. Initial Segmentation.* We apply adaptive thresholding<sup>10</sup> for the initial segmentation of the image  $R'$ . We first divide the image into several small non-overlapping blocks. The mean intensity of each block is chosen as the local threshold ( $T_{Local}$ ) for the segmentation. Assuming that the intensity of nuclei regions is lower than the background, we segment the image  $R'$  into foreground (represented by 1) and background (represented by 0) and obtain a binary image  $R^b$  as follows:

$$R^b(x, y) = \begin{cases} 1, & \text{if } R'(x, y) \leq T_{Local} \\ 0, & \text{otherwise} \end{cases} \quad (5)$$

By labeling the 8-connected component in the binary image  $R^b$ , we have the initial nuclei regions, denoted by  $\{H_q\}_{q=1 \dots n'}$ , where  $n$  is the number of potential nuclei regions. However, one potential problem identified is the presence of under-segmented regions mainly due to the local intensity variations. The under-segmentation problem is resolved by

using a finer segmentation module explained in the next section.

*2. Finer Segmentation for Local Regions.* In order to decompose the under-segmented regions, we incorporate 2 domain-specific knowledges: (a) the nuclei are elliptical-shape objects, and (b) the size of the nuclei region is within a predefined range  $[A_{min}, A_{max}]$ . The predefined range is determined from 1 prelabeled image. We label a region as an abnormally large region (ALR),  $H_r$ , if its area  $A(H_r)$  is greater than  $A_{max}$ . An ALR is considered as an under-segmented region and is further divided into subregions by minimizing a cost function. This is achieved as follows: (i) The dynamic range of the gray value in the ALR is first determined by assessing the highest and the lowest gray value of the ALR, and the dynamic range is denoted as  $[D_u, D_u]$ . (ii) Select a threshold  $t = D_u - j - 1$ , where  $j$  is the iteration number. Based on the threshold  $t$ , the ALR is segmented and the corresponding binary image  $B_t$  is obtained as follows:

$$B_t(x, y) = \begin{cases} 1, & \text{if } g(x, y) < t \\ 0, & \text{if } g(x, y) \geq t \end{cases} \quad (6)$$

where  $g(x, y)$  is the gray value of the ALR. (iii) Assume that the binary image  $B_t$  includes  $K$  disconnected regions, denoted by  $L_k$ ,  $1 \leq k \leq K$ . The point set of a region  $L_k$  and the point set of the corresponding best fitted ellipse is denoted by  $S(L_k)$  and  $\mathcal{E}(L_k)$ , respectively. The ellipticity penalty parameter  $\Phi_E$  for region  $L_k$  is calculated as follows:

$$\Phi_E(L_k) = \frac{|S(L_k) \Delta \mathcal{E}(L_k)|}{|\mathcal{E}(L_k)|} \quad (7)$$

where  $\Delta$  is the symmetric difference between two sets,  $|\cdot|$  is the cardinality of a point set. The best fitted ellipse for a region  $dc$  is computed using the direct least square fitting algorithm.<sup>11</sup> Note that  $\Phi_E(L_k) = 0$  if region  $L_k$  is an ideal ellipse. For region  $L_k$  with area  $A(L_k)$ , the area penalty parameter  $\Phi_A$  is calculated as follows:

$$\Phi_A(L_k) = \begin{cases} 0, & \text{if } A_{min} \leq A(L_k) \leq A_{max} \\ \frac{A_{min} - A(L_k)}{0.5(A_{min} + A_{max})}, & \text{if } 0 < A(L_k) < A_{min} \\ \frac{A(L_k) - A_{max}}{0.5(A_{min} + A_{max})}, & \text{if } A(L_k) > A_{max} \end{cases} \quad (8)$$

The penalty parameters  $\Phi_E$  and  $\Phi_A$  correspond to the 2 domain-specific items of knowledge, i.e., the shape and the size of nucleus. (iv) After calculating the 2 penalty parameters  $\Phi_E$  and  $\Phi_A$  for all  $K$  disconnected regions in the binary image  $B_r$ , a cost function  $C_r(t)$  is calculated for the current threshold  $t$  as follows:

$$C_r(t) = \frac{1}{K} \sum_{k=1}^K [\Phi_E(L_k) + \Phi_A(L_k)]. \quad (9)$$

Intuitively, the cost function  $C_r(t)$  is the accumulated penalty for all the  $K$  disconnected regions  $\{L_k\}_{k=1 \dots K}$  at threshold  $t$  for ALR  $H_r$ . If the segmented regions are close to the elliptical shapes and the segmented areas are within the predefined range  $[A_{min}, A_{max}]$ ,  $C_r(t)$  will have a small value. (v) For each possible threshold  $t \in [D_l, D_u]$ , we repeat the steps (ii) to (iv) to calculate the cost function  $C_r(t)$ . (vi) Determine the optimal threshold  $\tau_r$  for the ALR  $H_r$  by minimizing the cost function  $C_r(t)$ :

$$\tau_r = \arg_t \min[C_r(t)], t \in [D_l, D_u] \quad (10)$$

The  $B_r$  is the segmented result corresponding to the optimal threshold  $\tau_r$ . For each ALR the optimal threshold  $\tau_r$  is determined to decompose the ALR into subregions. Finally, the morphological opening based on blob-like structure is performed to remove tiny objects that are unlikely to be nuclei and smooth out all the regions.

#### Manual Identification of the Nuclei

In order to evaluate the performance provided by this new technique, the locations of nuclei and the boundaries of nuclei are manually labeled with the help of an interactive computer program (developed using MATLAB 7.1, MathWorks Inc., Natick, Massachusetts, U.S.A.). In the nuclei location manual labeling procedure, a marker that indicates 1 nucleus is recorded by the user mouse clicking operation in the computer program. Three examples of the markers with the images are shown in Figure 2b–e, where the bright dots indicate the manually labeled markers for the presence of nuclei. These manually identified locations are treated as the reference for the nuclei detection perform-

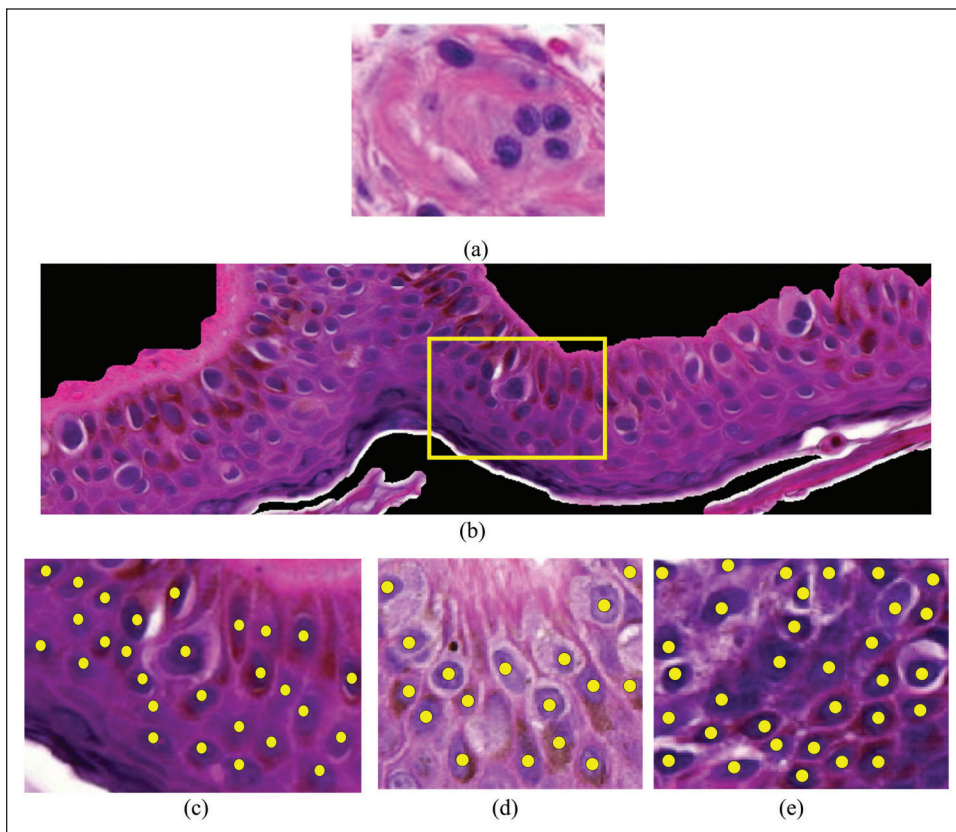


**Figure 2** H&E-stained histopathological images. (a) H&E-stained histopathological image (captured at 30x magnification). (b) The image of the epidermis area (captured at 20x magnification). (c) An image cropped from the highlighted area of (b). (d) and (e) are two additional H&E-stained images (captured at 30x magnification) from the skin epidermis. Note the inter- and intra-image variation of color. The bright dots indicate the location of nuclei.

ance evaluation. In total, there are 3,381 manually marked nuclei in 30 test images.

In the manual nuclei boundary labeling procedure, the contour of a nucleus representing the boundary is recorded by the user mouse clicking operation in the computer program. Two examples of the nuclei contours with the images are shown in Figure 3d, where the dotted contours indicate the manually labeled boundaries for the presence of nuclei. These manually identified boundaries are treated as the reference for the nuclei segmentation performance evaluation. Since it is time-consuming and tedious to label the boundaries for all 3,381 nuclei, 110 randomly selected nuclei boundaries are labeled and will be used in the nuclei segmentation performance evaluation.

#### Evaluation Metrics

The main objective of the evaluation is to determine if the segmented regions obtained by the proposed technique are consistent with the manually labeled ones. The nuclei segmentation results are provided with a binary image, where white regions indicate the nuclei regions. We perform 2 kinds of evaluations: the nuclei detection evaluation and nuclei segmentation evaluation.

*1. Detection Performance Evaluation.* For the detection performance evaluation we calculate the centroid of each segmented region obtained by the technique. A segmented nuclei region is counted as correctly detected if its centroid is localized within

a range of 5 pixels of the manually labeled nucleus location.

We define  $N_{ML}$  as the total number of manual labeled nuclei locations,  $N_{DO}$  as the total number of detected nuclei,  $N_{TP}$  as the number of true-positives, (i.e., correctly detected objects compared to the manually labeled nuclei locations),  $N_{FP}$  as the number of false-positives. (i.e., falsely detected objects compared to the manual labeled nuclei locations), and  $N_{US}$  as the number of nuclei that are under-segmented.

The performance is evaluated with respect to the positive predictive value (PPV), sensitivity (SEN), and under-segmentation rate (USR) which are defined as follows:

$$PPV = \frac{N_{TP}}{N_{DO}} \times 100\% \quad (11)$$

$$SEN = \frac{N_{TP}}{N_{ML}} \times 100\% \quad (12)$$

$$USR = \frac{N_{US}}{N_{TP}} \times 100\% \quad (13)$$

The evaluation metric USR indicates cases where multiple nuclei are clubbed into a large region and result in degraded segmentation performance. A small USR value indicates less under-segmentation in the result, which is a desirable outcome.

*2. Segmentation Performance Evaluation.* For the segmentation performance evaluation, we compare

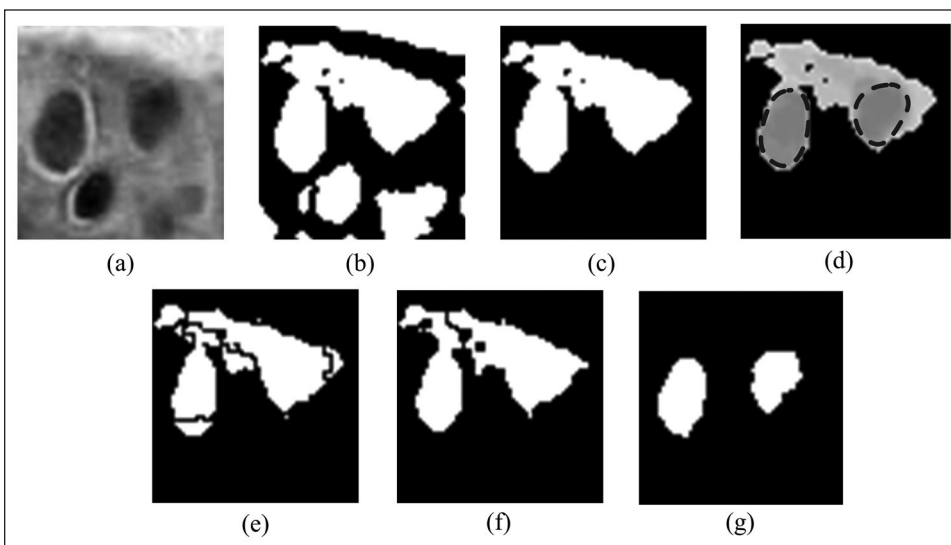


**Figure 3** Segmentation performance of the LRATS and watershed techniques. (a) The original image. (b) The binary image after threshold. (c) The ALR. (d) The red channel image (after HGMR) superimposed onto the binary image. (e) The segmentation result after applying the watershed. (f) The segmentation result after applying the marker-control watershed. (g) The segmentation result after applying the LRATS. Note that the dotted contours in (d) indicate the reference nuclei boundaries.

the area, perimeter and form factor of the nuclei obtained by the automatic technique and the manually labeled ones using the Bland-Altman plot.<sup>12,13</sup> The form factor is defined as follows:

$$F = \frac{4\pi A}{P^2} \quad (14)$$

where  $A$  and  $P$  represent the area and the perimeter of a nucleus, respectively. The Bland-Altman plot is widely used in comparing 2 measurements in terms of the agreement. In the Bland-Altman plot, the x-axis shows the average values of the 2 measurements, whereas the y-axis shows the difference of the 2 measurements. Mathematically, given a sample  $S$  and its 2 measurements  $\tilde{S}_1$  and  $\tilde{S}_2$ , we have a data point in the Bland-Altman plot which is defined as follows:

$$S(x,y) = \left( \frac{\tilde{S}_1 - \tilde{S}_2}{2}, (\tilde{S}_1 - \tilde{S}_2) \right). \quad (15)$$

In our evaluation we set the limits of agreement as the bias (mean)  $\pm 1.96$  standard deviation of the difference between 2 measurements.

## Results

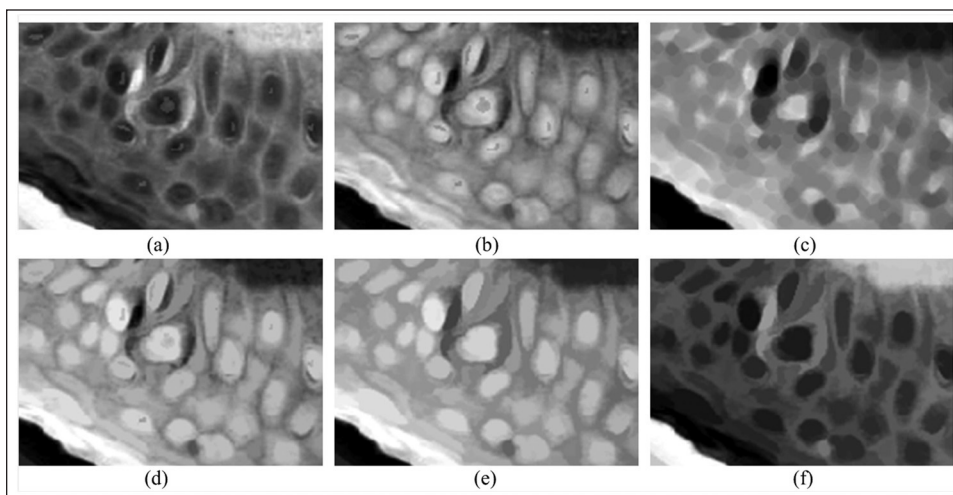
### Intermediate Results of the HGMR Module

Figure 4 presented the intermediate results obtained by the HGMR module of the proposed technique. Figure 4a is an original H&E-stained image containing several nuclei. Figure 4b shows the complement image of Figure 4a. The eroded image obtained by applying erosion on Figure 4b is shown in Figure 4c. The result of the *open-by-reconstruction* is

shown in Figure 4d. Comparing Figures 4d and 4b, the nuclei regions have been enhanced. The result of the *closing-by-reconstruction* is shown in Figure 4e. It shows that the intensity within the nuclei regions is more homogenous compared to that in Figure 4d. By comparing Figures 4a and 4f, it is observed that the HGMR is able to make the nuclei regions more homogenous for the subsequent nuclei segmentation operations.

### Intermediate Results of the LRATS Module

Figure 5 presents the intermediate results obtained by the LRATS module of the proposed technique. Figure 5a shows the segmented image obtained by applying initial segmentation on the image in Figure 4f. For better visualization we superimpose the original image onto the binary image. The results show that most of the nuclei are segmented correctly. However, due to the local intensity variation, there are a few under-segmented regions (highlighted by the solid bright contours in Figure 5a). Figure 5b shows an ALR from Figure 5a where under-segmentation is present. Figure 5c is the cost function value computed using Eq. 9. The minimum value is pointed out with an arrow. The optimal threshold is  $\tau_r = 84$ . Figure 5d shows the sub-regions  $\{L_k\}_{k=1\dots K}$  corresponding to the optimal threshold  $\tau_r$ . It is observed that the cost function value is significantly decreased when the intensity threshold is  $t \approx 95$ . When the threshold is  $t \approx 95$ , the ALR broken into many subregions and the corresponding area penalty parameter is equal to zero. As a result, the value of the cost function is only determined by the ellipticity penalty parameter. The



**Figure 4** Illustration of the hybrid gray-scale morphological reconstruction.

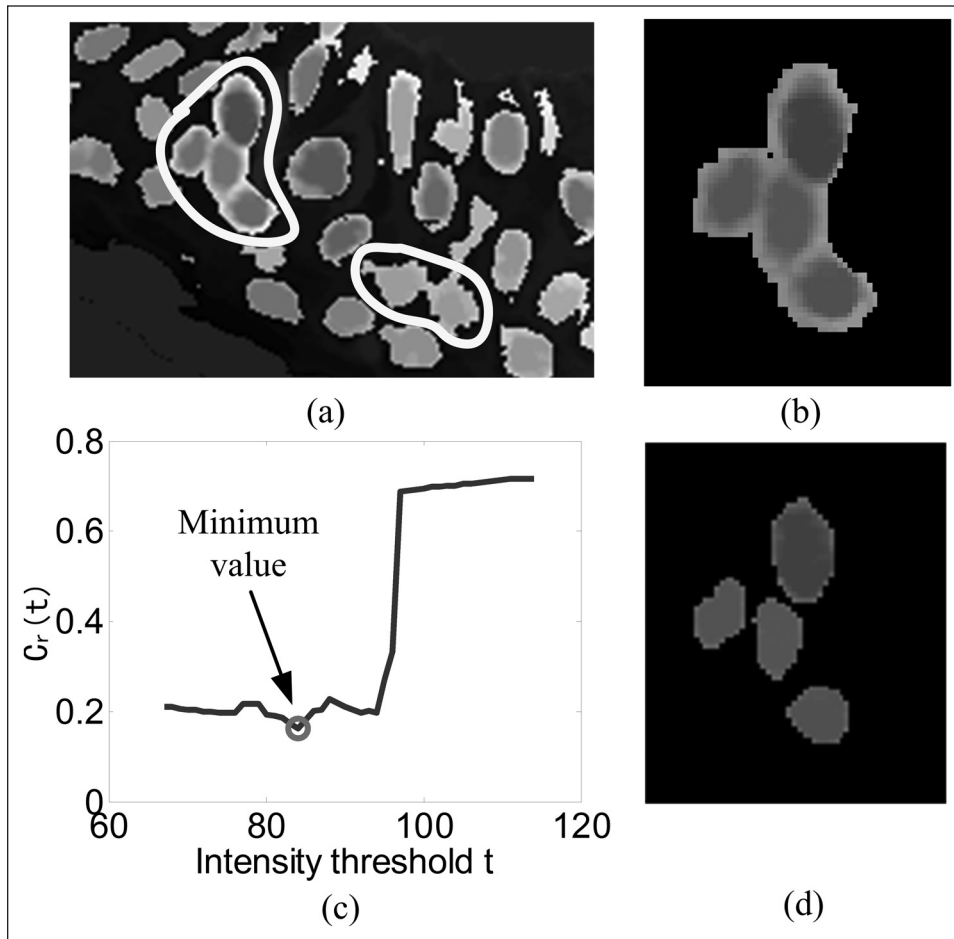


**Figure 5** Segmentation of nuclei using LRATS. (a) The initial segmented image corresponding to Figure 4f. (b) A magnified ALR from (a). (c) The plot of the cost function. (d) The subregions segmented by the optimal threshold  $t_r$ .

final result of the nuclei segmentation corresponding to Figure 5a is shown in Figure 6e.

#### Final Results of the Proposed Technique

Three examples of the final results obtained by the proposed technique are shown in Figure 7. The first row shows 3 original H&E-stained images whereas the second row shows the corresponding segmentation results (the white regions indicate the nuclei regions and the dots indicate the manually labeled nuclei locations). It shows that most of the nuclei regions are recovered by the proposed technique and only a few nuclei regions are missed in images where significant intensity variations are present.

We use the evaluation metric introduced in Section II-F to evaluate the detection performance of proposed technique for 3,381 nuclei in 30 images captured under 30 $\times$  magnification. The proposed technique achieves 80.02% PPV, 88.11% SEN and 5.34% USR.

The segmentation performance in terms of nucleus area, perimeter and form factor are shown in Figures 8d, 9d and 10d, respectively. Each figure shows Bland-Altman plot between the result obtained by the proposed technique and the manually labeled nuclei region. It shows that the proposed technique is able to provide consistent segmentation results compared to the manual segmentation.

#### Discussion

Traditionally, the histopathological sections for microscopic analysis are primarily stained with H&E. These sections allow anatomical pathologists to assess a wide range of specimens obtained from biopsies and surgical procedures. Further studies (such as special stains, immunohistochemical stains and other ancillary studies) can be employed to augment the diagnoses; however, H&E-stained slides still play the most important role in histopathological evaluation. In order to further enhance the

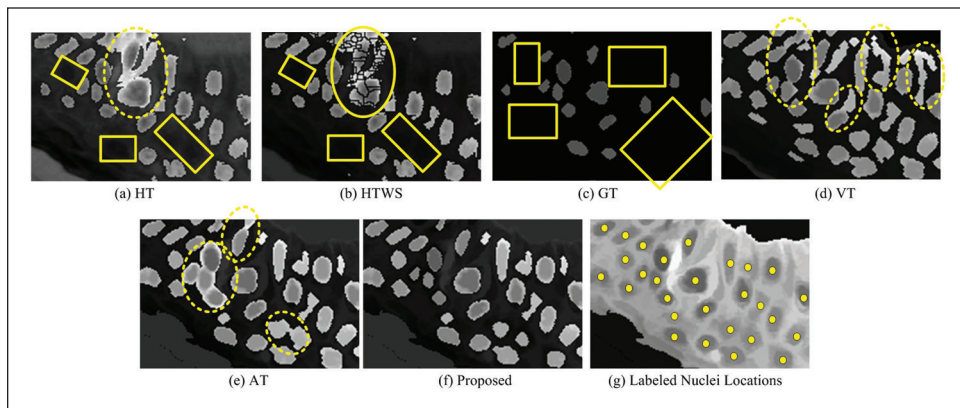


**Figure 6** Performance comparison of the nuclei segmentation techniques. The segmentation results are shown as brighter regions in each image. The bright dots in (g) indicate the manually labeled nuclei locations. The under-segmentation is indicated by the dotted lines, and the miss detection of nuclei are indicated by the solid rectangles.

microscopic analysis, many computer-aided image analysis techniques have been proposed. However, certain obstacles and limitations still exist in achieving a good result. Figure 2a shows one example of an H&E-stained histopathological image. In this image the cell nuclei are stained as blue-purple due to hematoxylin, whereas the cell membranes and cytoplasmic contents are stained as pink since its contents absorb the staining dye eosin. In this image the nuclei (i.e., foreground) and the cytoplasmic contents (i.e., background) have acceptable discrimination. However, a wide variety of reasons (e.g., tissue fixation, staining method employed, specimen type, etc.) may lead to nonuniform staining variations and complex backgrounds. Intra-image and inter-image variations exist and color/intensity

values of the foreground and background may appear similar. Figures 2b-e show examples of H&E-stained histopathological images of cutaneous epidermis. In Figure 2b nonuniform staining variation exists, i.e., the color/intensity value of cytoplasm around the rectangular area is lower than the other areas. For better visualization, a magnified version of the rectangular region is shown in Figure 2c. Two other images captured from the epidermis are shown in Figures 2d and 2e. The ground truth nuclei are indicated with bright dots in Figures 2c-2e. The presence of staining variations (intra-image and inter-image) and similar backgrounds can pose as obstacles for accurate segmentation of the nuclei in histopathological images. In this study we propose an effective technique for segmentation of

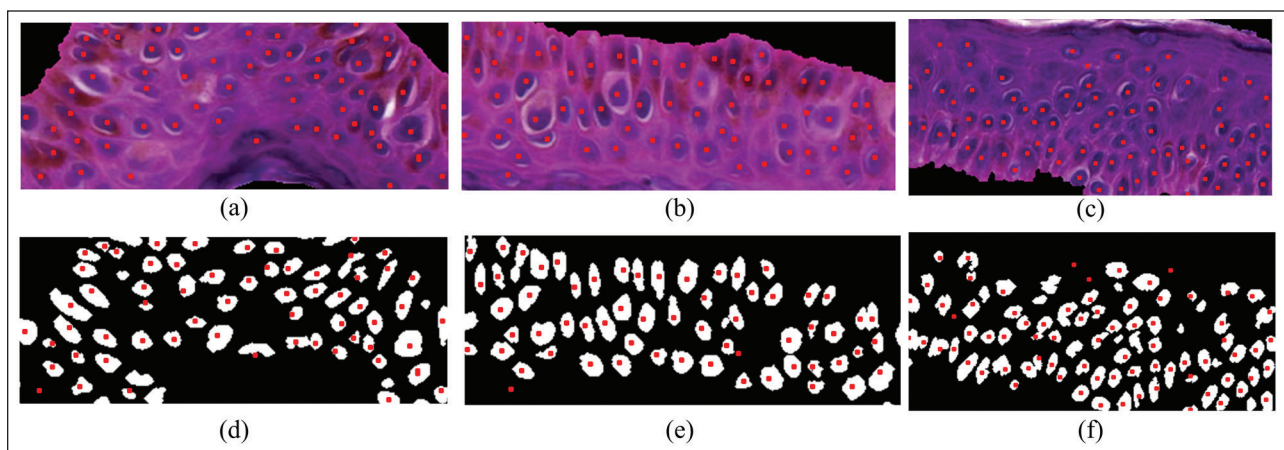


**Figure 7** Final results obtained by the proposed technique. (a), (b) and (c) show the original H&E-stained images (original magnification at 30×). The manually labeled nuclei locations are shown as red dots on the image. (d), (e) and (f) show the final segmentation results (binary images where the white regions indicate the nuclei regions) corresponding to (a), (b) and (c), respectively. The manually labeled nuclei locations are also shown on the images for comparison purpose.

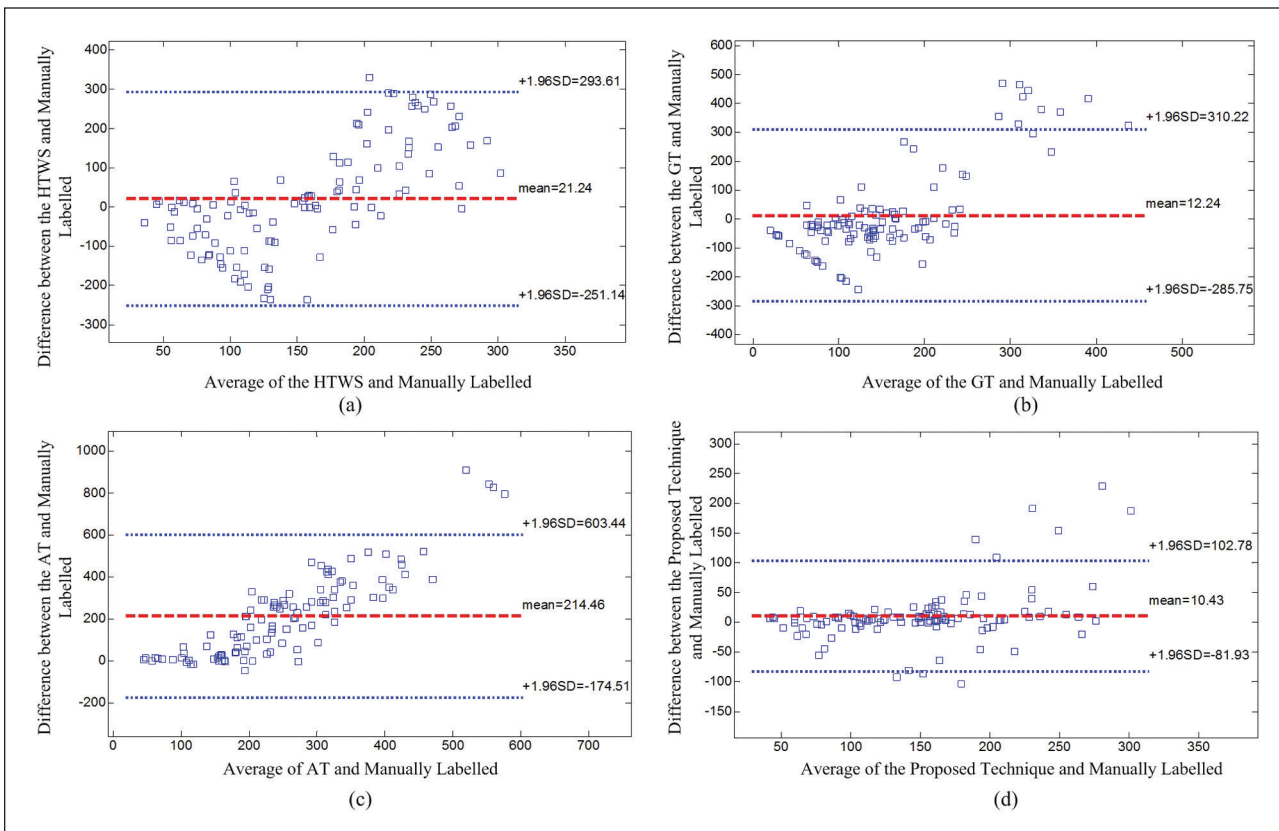


**Figure 8** Segmentation performance comparison of the nuclei segmentation techniques in terms of nucleus area. (a) Bland-Altman plot of 110 nuclei areas obtained by the HTWS and the manually labeled ones. (b) Bland-Altman plot of 110 nuclei areas obtained by the GT and the manually labeled ones. (c) Bland-Altman plot of 110 nuclei areas obtained by the AT and the manually labeled one. (d) Bland-Altman plot of 110 nuclei areas obtained by the proposed technique and the manually labeled ones. The mean of the difference is shown as the thick dash line whereas the limits of agreement (mean  $\pm$  STD of difference) are shown as the dotted lines.

nuclei from histopathological images. Our technique tries to overcome limitations and obstacles usually faced in accurate nuclei segmentation and aims to provide superior performance. In this section we will discuss the efficiency of the proposed technique by comparing it with other available techniques.

#### Comparison with Other Techniques

In this subsection, we compare the proposed technique with other threshold-based techniques: HTWS,<sup>4</sup> GT,<sup>1</sup> AT,<sup>5</sup> and a variational-based adaptive threshold technique (VT).<sup>14</sup> The HTWS technique first employs the *top-hat by reconstruction* operation to reduce the background signal in the image. The hysteresis threshold method is then used to perform the segmentation. The hysteresis threshold method uses 2 thresholds in order to avoid the disconnected

segmentation results where local variations are present. In the end, the watershed method<sup>15</sup> is used to reduce the under-segmentation. For the HTWS technique we first evaluate the performance using only the hysteresis technique (HT). We then evaluate the whole HTWS technique, which uses the watershed method after the HT.

In the HT the upper and lower (gray value) thresholds are set to 100 and 80, respectively. In the evaluation we apply the watershed method on the ALR selected by a predefined area threshold. In the GT technique the global threshold is set to  $0.3 \times G_H$ , where  $G_H$  is the highest gray value in the image. In the AT technique the local threshold is computed for each nonoverlap block in the whole image using the mean intensity value. In the AT technique the window size is set to  $40 \times 40$  pixels. For all the compared techniques we selected the parameters such

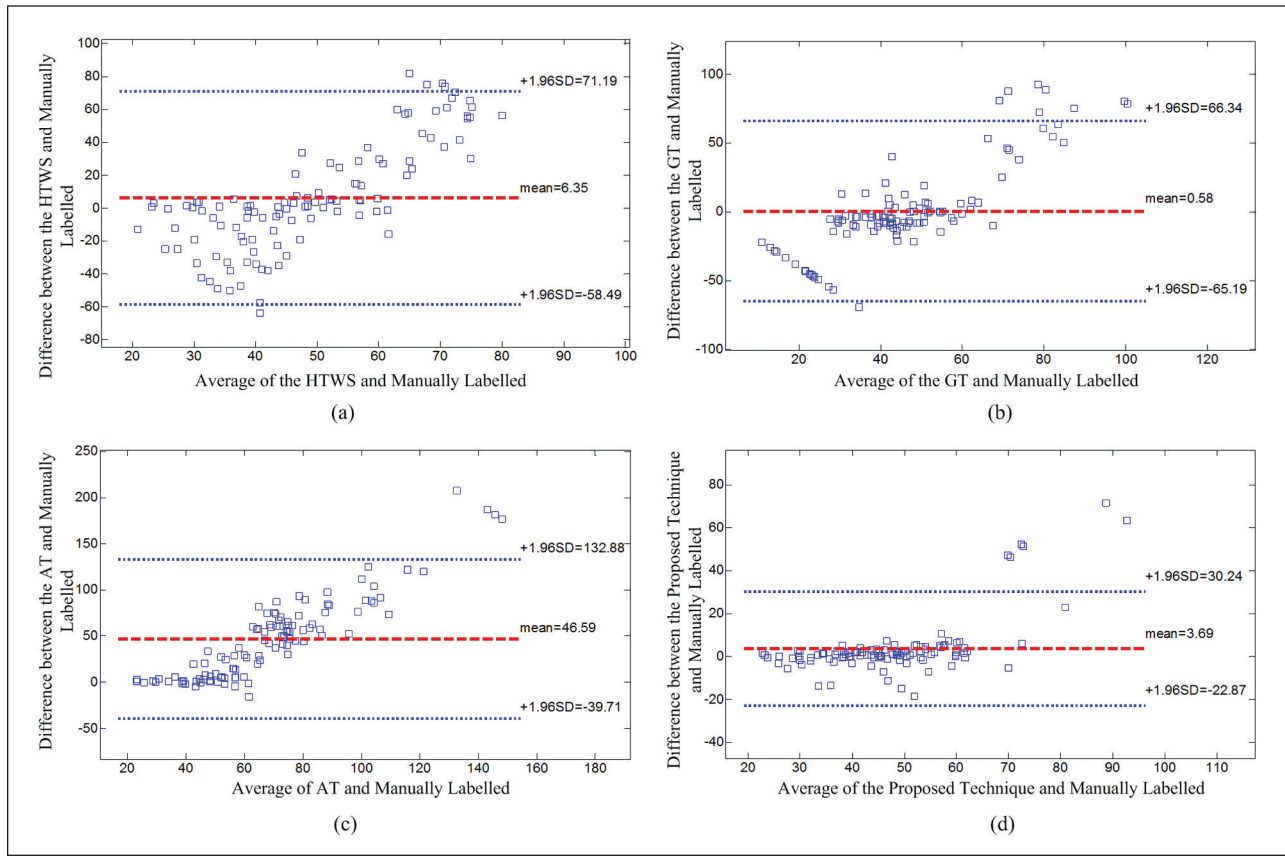


**Figure 9** Segmentation performance comparison of the nuclei segmentation techniques in terms of nucleus perimeter. (a) Bland-Altman plot of 110 nuclei areas obtained by the HTWS and the manually labeled ones. (b) Bland-Altman plot of 110 nuclei perimeters obtained by the GT and the manually labeled ones. (c) Bland-Altman plot of 110 nuclei perimeters obtained by the AT and the manually labeled one. (d) Bland-Altman plot of 110 nuclei perimeters obtained by the proposed technique and the manually labeled ones.

that the best segmentation result is achieved. For our proposed technique the window size for the initial segmentation is set to  $40 \times 40$  pixels, and the range of size of the nuclei regions is set to  $A_{min} = 100$  and  $A_{max} = 500$ .

**1. Detection Performance Comparison.** The detection performance comparison of the threshold-based techniques is shown in Table I (using the evaluation metrics introduced in Section II-F). It shows that the HT technique results in a high USR (about 49%). This is due mainly to local cell clustering in epidermis with intensity variations. In order to reduce the under-segmentation, the watershed method is applied on the ALR in the HTWS technique. The corresponding performance is shown in the third row of Table I. USR of the HTWS is reduced to 9.85%. However, due to the intensity variation the water-

shed method leads to over-segmentation and the PPV is very low (25.98%).

In the case of GT, as it uses a single threshold, it misses most of the nuclei regions that have higher intensity values. This results in a very low SEN (48.98%). The AT technique uses local thresholds to perform the nuclei segmentation and achieves better SEN than the HT, HTWS and GT techniques. However, it still cannot separate the clustered nuclei regions, which results in high USR at 35.11%. The VT technique calculates a smooth threshold surface that encourages the intersection with the image surface at the edge. The VT technique provides high SEN (87.31%) and relatively low USR (14.74%). However, it leads to low PPV (66.17%), which is mainly due to the complex background. Our proposed technique achieves the lowest USR (5%), which reflects the effectiveness of the LRATS

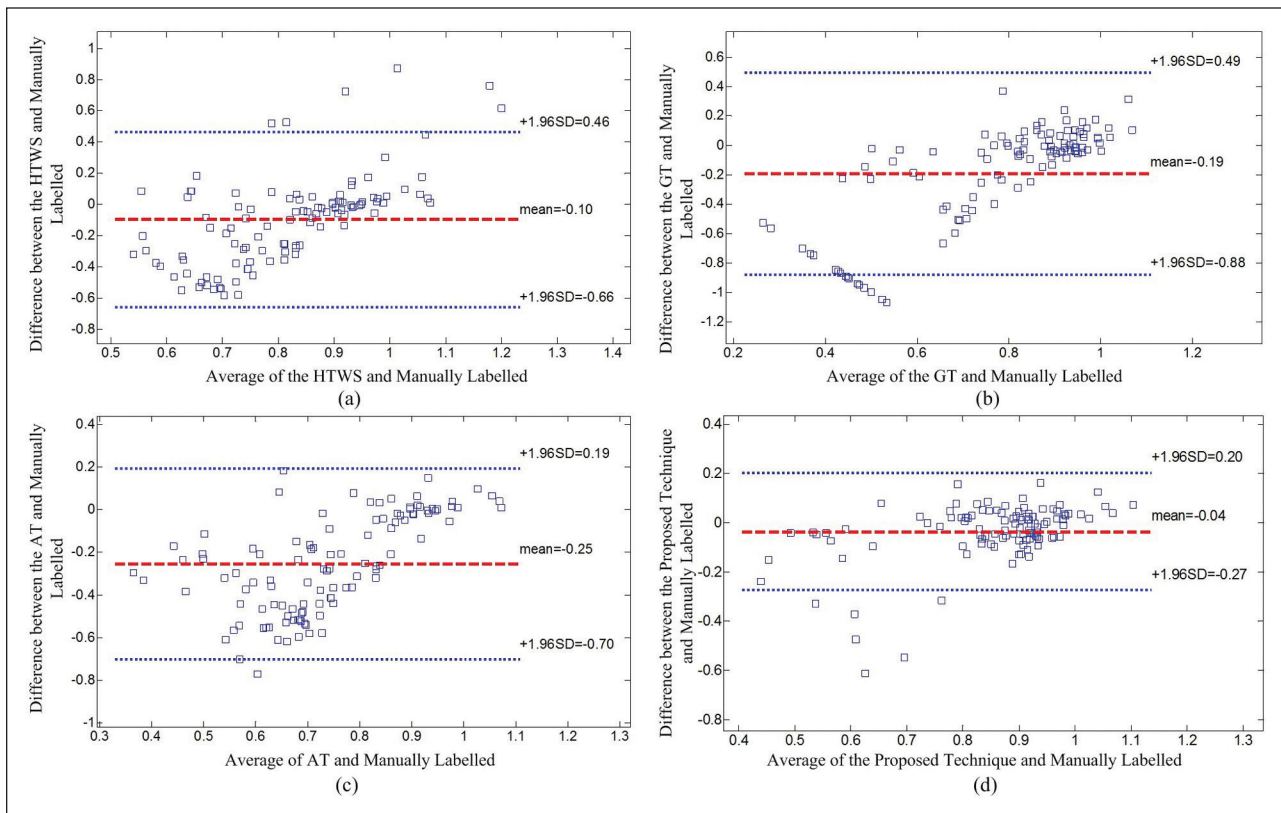


**Figure 10** Segmentation performance comparison of the nuclei segmentation techniques in terms of nucleus form factor. (a) Bland-Altman plot of 110 nuclei form factors obtained by the HTWS and the manually labeled ones. (b) Bland-Altman plot of 110 nuclei form factors obtained by the GT and the manually labeled ones. (c) Bland-Altman plot of 110 nuclei form factors obtained by the AT and the manually labeled one. (d) Bland-Altman plot of 110 nuclei form factors obtained by the proposed technique and the manually labeled ones.

module for segmenting the ALR. Also, our proposed technique has the highest SEN (about 88%) and a high PPV (about 80%) compared to other techniques.

Figure 6 illustrates the subjective performance comparison of the nuclei segmentation techniques. In the subjective performance comparison the segmentation results (shown as brighter regions) are compared to the manually labeled nuclei locations. A segmentation result that provides intact nuclei regions and fewer under-segmentation regions is desired. The original image is shown in Figure 2b. The segmentation results obtained by the HT,<sup>4</sup> HTWS,<sup>4</sup> GT,<sup>1</sup> VT,<sup>14</sup> AT<sup>5</sup> and our proposed technique are shown in Figures 6a-f, respectively. The red channel image is superimposed onto the segmentation result for better visualization.

The HT technique produces under-segmentation that is indicated by the dotted ellipse in Figure 6a.

Also, some of the nuclei are not detected by the HT technique (e.g., in the regions indicated by the solid rectangles). In the HTWS technique the watershed method is applied to the ALR that is indicated by the dotted ellipse in Figure 6a. The corresponding result is shown in Figure 6b. It is clear that the region is breaking into several small regions that lead

**Table I** Performance Evaluations of the Proposed Technique with Other Existing Techniques on Skin Epidermis Images

Techniques	NML	PPV (%)	SEN (%)	USR (%)
HT4	3,381	71.00	69.30	49.04
HTWS4	3,381	25.98	71.16	9.85
GT1	3,381	84.66	48.98	22.28
AT5	3,381	80.34	80.12	35.11
VT14	3,381	66.17	87.31	14.74
Proposed	3,381	80.02	88.11	5.34

to over-segmentation. In Figure 6c the GT technique misses many of the nuclei regions (indicated by the solid rectangles). The main reason appears to be that the GT technique considers only 1 global threshold and the nuclei regions that have higher intensity are missed. In Figure 6d the result obtained by the VT technique includes many background regions due to the complex background (indicated by the dotted ellipses in Figure 6d). The AT technique uses different thresholds depending on local characteristics and appears to provide a better performance. However, under-segmentation still exists (shown in the 3 dotted ellipses in Figure 6e). It appears that our proposed technique reduces the under-segmentation successfully while keeping all the nuclei segmented (shown in Figure 6f).

**2. Segmentation Performance Comparison.** In this subsection we present the segmentation performance of the automatic techniques and compare it with the manually labeled nuclei regions using the Bland-Altman plot. The automatic techniques include the existing techniques for nuclei segmentation (i.e., the HTWS, GT and AT techniques) and the proposed technique. The automatic segmented nuclei measurements obtained by the automatic techniques compared to the manually labeled ones in terms of the area, perimeter and the form factor are shown in Figures 8, 9 and 10, respectively. These results show that the measurements of the automatic segmented nuclei obtained by the proposed technique are more consistent with the manually labeled ones (with smaller mean values and standard derivation (SD) compared to that of other existing techniques).

#### *Comparison between the Proposed LRATS and the Watershed Methods*

We compared the segmentation performance of the LRATS module of our proposed technique and the widely used watershed segmentation method for nuclei segmentation.<sup>4</sup> Figure 3 shows an example for the performance comparison. An original red channel image is shown in Figure 3a. Following the initial segmentation by using a threshold, we obtained the binary segmented image shown in Figure 3b. Due to the complex background the initial segmentation result includes some background regions that have low intensity value. We were primarily concerned about the ALR shown in Figure 3c. In Figure 3d the red channel image (after HGMR) is superimposed onto the binary image for

better visualization. In this ALR two nuclei regions exist, and they are indicated by the 2 dotted contours. The pixels outside the 2 dotted contours belong to the background. If we applied the watershed method on this ALR, we obtained an over-segmentation result as shown in Figure 3e. In the watershed method the local regional minimums were first determined as the basins for the segmentation.<sup>10</sup> An incorrect number of local regional minimums will lead to over-segmentation. However, even though we knew the exact number and the location of the nuclei in this ALR, we still obtained inaccurate results. This is illustrated in Figure 3f. Figure 3f presents the result obtained using the marker-control watershed method, where the markers for the 2 nuclei are specified by human interaction. Note that the number of the segmented regions is correct, i.e., 2 segmented regions are obtained from the original ALR. However, in each region there still exists the background region that does not belong to the nucleus. On the other hand, the segmented regions obtained by the proposed LRATS are accurate and do not contain redundant regions that belong to the background (Figure 3g). This illustrates the effectiveness of the proposed LRATS compared to the watershed method. In summary, our study presents a novel computer-aided technique for segmentation of the nuclei in histopathological images. The intraobject variations are first reduced by using the hybrid morphological reconstructions. A novel threshold selection algorithm for local regions is then used to segment the nuclei. By incorporating the domain-specific knowledge, this technique reduces the under-segmentation of the nuclei and provides a superior performance compared to the existing techniques. The evaluation on H&E-stained histopathological skin epidermis images (containing >3,300 nuclei) shows the effectiveness of the technique. Although the technique has been evaluated for the nuclei segmentation in skin histopathological images, it can be applied to nuclei segmentation in other organs.

#### **References**

1. Korde VR, Bartels H, Barton J, Ranger-Moore J: Automatic segmentation of cell nuclei in bladder and skin tissue for karyometric analysis. *Anal Quant Cytol Histol* 2009;31:83–89
2. Fuchs TJ, Buhmann JM: Computational pathology: Challenges and promises for tissue analysis. *Comput Med Imaging Graph* 2011;35:515–530
3. Gurcan MN, Boucheron LE, Can A, Madabhushi A, Rajpoot NM, Yener B: Histopathological image analysis: A review. *IEEE J Rev Biomed Eng* 2009;2:147–171

4. Gurcan M, Pan T, Shimada H, Saltz J: Image analysis for neuroblastoma classification: Segmentation of cell nuclei. *Conf Proc IEEE Eng Med Biol Soc* 2006;1:4844–4847
5. Petushi S, Garcia FU, Haber MM, Katsinis C, Tozeren A: Large-scale computations on histology images reveal graded-differentiating parameters for breast cancer. *BMC Med Imaging* 2006;6:14
6. Naik S, Doyle S, Feldman M, Tomaszewski J, Madabhushi A: Gland segmentation and computerized Gleason grading of prostate histology by integrating low-, high-level and domain specific information. In: Proceedings of 2nd Workshop on Microscope Image Analysis with Applications in Biology. Piscataway, New Jersey, USA, 2007
7. Sertel O, Catalyurek U, Shimada H, Guican M: Computer-aided prognosis of neuroblastoma: Detection of mitosis and karyorrhexis cells in digitized histological images. *Conf Proc IEEE Eng Med Biol Soc* 2009;2009:1433–1436
8. Basavanhally AN, Ganesan S, Agner S, Monaco JP, Feldman MD, Tomaszewski JE, Bhanot G, Madabhushi A: Computerized image-based detection and grading of lymphocytic infiltration in HER2+ breast cancer histopathology. *IEEE Trans Biomed Eng* 2010;57:642–653
9. Fatakddwala H, Xu J, Basavanhally A, Bhanot G, Ganesan S, Feldman M, Tomaszewski J, Madabhushi A: Expectation-maximization-driven geodesic active contour with overlap resolution (EMaGACOR): Application to lymphocyte segmentation on breast cancer histopathology. *IEEE Trans Biomed Eng* 2010;57:1676–1689
10. Gonzalez R, Woods R: Digital image processing, 2002
11. Fitzgibbon M, Pilu AW, Fisher RB: Direct least-squares fitting of ellipses. *IEEE Trans Pattern Anal Mach Intell* 1999;21: 476–480
12. Altman DG, Bland JM: Measurement in medicine: The analysis of method comparison studies. *The Statistician* 1983;32: 307–317
13. Hanneman S: Design, analysis and interpretation of method-comparison studies. *AACN Adv Crit Care* 2008;19:223
14. Saha B, Ray N: Image thresholding by variational minimax optimization. *Pattern Recognition* 2009;42:843–856
15. Vincent L, Soille P: Watersheds in digital spaces: An efficient algorithm based on immersion simulations. *IEEE Trans Pattern Anal Mach Intell* 1991;13:583–598